2019

Mechanically transformative electronics, sensors, and implantable devices

Sang-Hyuk Byun

Marie C Walicki

Kyle E Parker

Graydon B Gereau

John Bilbily

See next page for additional authors

Authors
Sang-Hyuk Byun, Marie C Walicki, Kyle E Parker, Graydon B Gereau, John Bilbily, Jordan G McCall, and et al

APPLIED SCIENCES AND ENGINEERING

Mechanically transformative electronics, sensors, and implantable devices

Sang-Hyuk Byun[1]*, Joo Yong Sim[2]*, Zhanan Zhou[3], Juhyun Lee[1], Raza Qazi[1,4], Marie C. Walicki[5,6,7,8], Kyle E. Parker[5,6,7,8], Matthew P. Haney[4], Su Hwan Choi[1], Ahnsei Shon[4], Graydon B. Gereau[5,6,7,8], John Bilbily[5,6,7,8,9], Shuo Li[10], Yuhao Liu[4], Woon-Hong Yeo[11], Jordan G. McCall[5,6,7,8], Jianliang Xiao[3], Jae-Woong Jeong[1,4†]

Traditionally, electronics have been designed with static form factors to serve designated purposes. This approach has been an optimal direction for maintaining the overall device performance and reliability for targeted applications. However, electronics capable of changing their shape, flexibility, and stretchability will enable versatile and accommodating systems for more diverse applications. Here, we report design concepts, materials, physics, and manufacturing strategies that enable these reconfigurable electronic systems based on temperature-triggered tuning of mechanical characteristics of device platforms. We applied this technology to create personal electronics with variable stiffness and stretchability, a pressure sensor with tunable bandwidth and sensitivity, and a neural probe that softens upon integration with brain tissue. Together, these types of transformative electronics will substantially broaden the use of electronics for wearable and implantable applications.

INTRODUCTION

Nearly all modern electronics, including both conventional rigid consumer electronics and emerging soft electronics (*1*–*6*), have invariant mechanical properties to serve specific purposes. Flat, rigid electronics provide user-friendly, convenient solid interfaces that maximize the convenience of use in a tabletop or handheld setup. Soft, flexible, and stretchable electronics are better suited for wearable and implantable applications (*1*–*6*), where their ability to accommodate natural deformation of bodily tissue can substantially improve comfort, portability, and ease of continuous physiological monitoring. However, the static mechanical nature of both rigid and flexible electronics limits the applications of these devices. For example, mounting conventional rigid electronics on the skin creates a mechanical mismatch between the bulky, hard components of the device and the soft tissue, making them unconformable and inconvenient to wear. Likewise, the use of soft electronics for off-body applications can lead to difficulties in handling and interfacing due to the device's inability to withstand high contact forces and loads.

To leverage key features of both traditional flat, rigid electronics and emerging soft electronics, we introduce a new class of electronic systems that can transform their shape and stiffness as necessary for desired applications. We enabled this feature based on temperature-triggered soft-rigid phase transition of mechanically tunable electronics platforms. The approach reported here can make electronics more versatile, convenient, and highly adaptive to various applications. We demonstrate various transformative electronics using this phase-transition strategy, including a handheld device convertible to a stretchable wearable device, a pressure sensor with tunable bandwidth and sensitivity, and a rigid neural probe that softens upon injection into the brain. These are only a few examples that can be achieved with this transformative platform technology, and we anticipate that many more will be enabled.

RESULTS

Design, materials, and mechanics

Figure 1 (A and B) and fig. S1 show schematic illustrations and optical images of a demonstrative electronic system that can be held or used much like a traditional consumer electronics such as a laptop or a smartphone but that can also spontaneously soften, stretch, and curve upon mounting onto the skin to measure electrophysiological signals from the body. This system, which we refer to as a "transformative electronic system" (TES), integrates flexible, stretchable electronics with serpentine metal interconnects (*1*, *4*) onto a transformative platform made using a composite of gallium (99.99%) and soft, biocompatible silicone encapsulant (Ecoflex, Smooth-On; ~60 kPa), which can reconfigure its shape, stiffness, and stretchability through a temperature-dependent phase transition (Fig. 1B). We can construct such gallium-elastomer composite transformative platforms either by encapsulating a gallium frame with an elastomeric polymer (Fig. 1B) or by mixing gallium microdroplets with the elastomer.

Among many phase change materials (*7*–*20*), including shape memory polymers (*7*–*9*, *20*), phase change metals (e.g., low–melting point alloys) (*10*–*13*), and magnetorheological (*14*, *15*) and electrorheological fluids (*16*), gallium is one of the most attractive options for the transformative platform involving biological applications because of its biocompatibility, high elastic modulus (9.8 GPa), and ideal

[1]School of Electrical Engineering, Korea Advanced Institute of Science and Technology (KAIST), Daejeon 34141, Republic of Korea. [2]Welfare & Medical ICT Research Department, Electronics and Telecommunications Research Institute, Daejeon 34129, Republic of Korea. [3]Department of Mechanical Engineering, University of Colorado Boulder, Boulder, CO 80309, USA. [4]Department of Electrical, Computer, and Energy Engineering, University of Colorado Boulder, Boulder, CO 80309, USA. [5]Department of Anesthesiology, Washington University in St. Louis, St. Louis, MO 63110, USA. [6]Department of Pharmaceutical and Administrative Sciences, St. Louis College of Pharmacy, St. Louis, MO 63110, USA. [7]Center for Clinical Pharmacology, St. Louis College of Pharmacy and Washington University School of Medicine, St. Louis, MO 63110, USA. [8]Washington University Pain Center, Washington University in St. Louis, St. Louis, MO 63110, USA. [9]Department of Psychiatry, Washington University in St. Louis, St. Louis, MO 63110, USA. [10]Department of Materials Science and Engineering, Cornell University, Ithaca, NY 14853, USA. [11]George W. Woodruff School of Mechanical Engineering and Wallace H. Coulter Department of Biomedical Engineering, Georgia Institute of Technology, Atlanta, GA 30332, USA.
*These authors contributed equally to this work.
†Corresponding author. Email: jjeong1@kaist.ac.kr

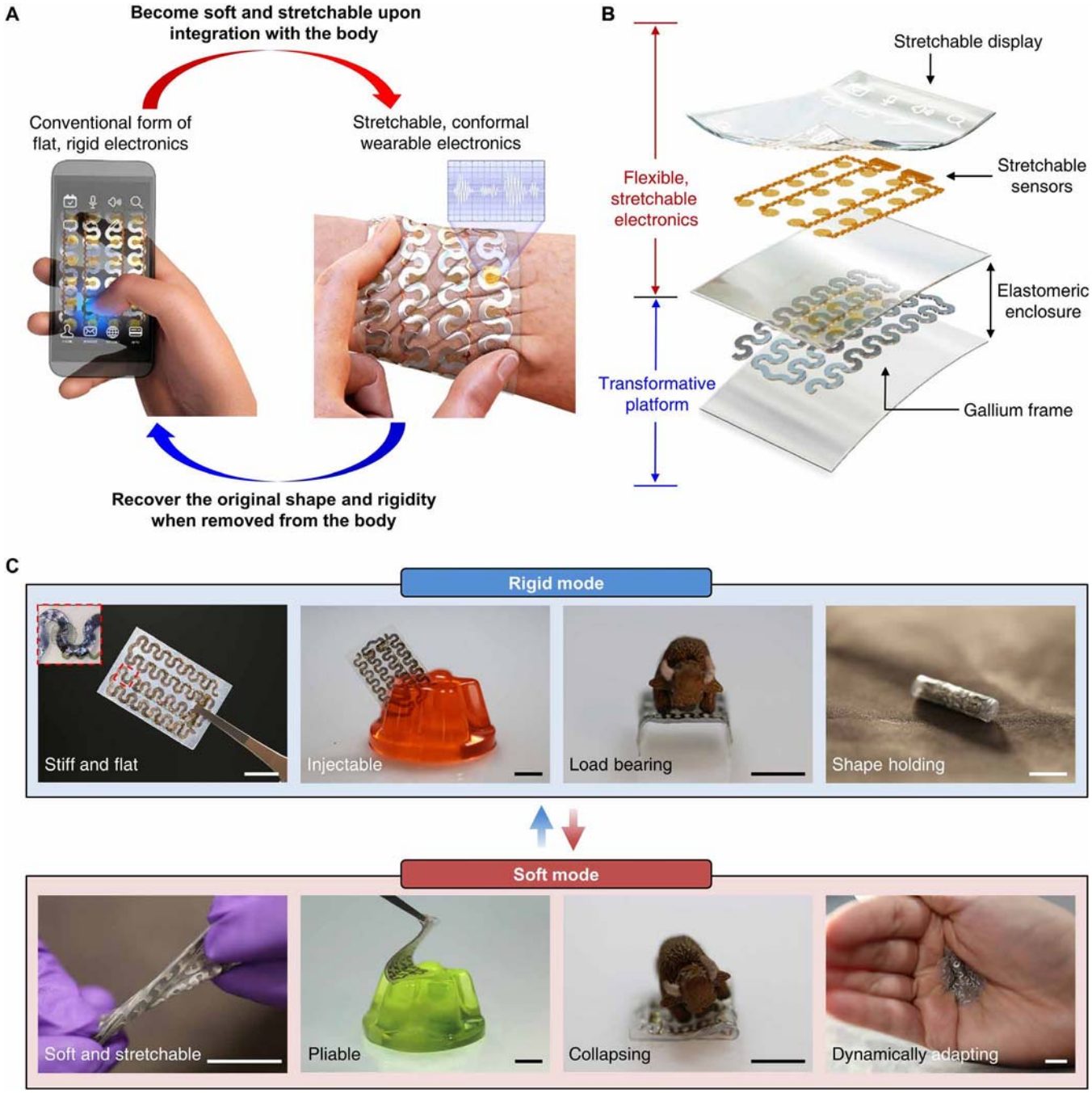

Fig. 1. Schematic illustrations and images of a TES that can shift its form from a conventional rigid electronic device to a soft, stretchable electronics format, or vice versa, through a temperature-dependent phase transition. (**A**) Conceptual illustration of the key feature of the system. A flat, rigid, and handheld electronic device becomes soft and stretchable upon integration onto the skin due to the effect of body temperature and thus converts into a wearable device that can measure physiological signals [e.g., electromyogram (EMG) and electrocardiogram]. Similarly, the device can recover its original rigidity when removed from the body to decrease its temperature. (**B**) Exploded-view schematic diagram illustrating the system architecture. (**C**) Images of a TES demonstrating its mechanical characteristics in the rigid (top) and soft (bottom) mode. The inset of the far left image in the rigid mode shows a magnified view of the region indicated by the red dashed box, highlighting a stretchable gold electrode integrated with the gallium-based transformative platform. Scale bars, 1 cm. Photo credit: Jae-Woong Jeong.

melting temperature (29.8°C) (*21*, *22*), which makes it solid at room temperature (22° to 25°C) and liquid at the temperature of biological tissue (32° to 37°C). By being embedded in a soft polymer, similar to what have been reported by recent studies on variable stiffness devices (*10*, *12*, *23*), the meltable and freezable features of gallium enable large rigidity tuning (between a few tens of kPa and ~10 GPa) when applied to or detached from tissue. That is, a TES fabricated with gallium can be rigid at room temperature or below but becomes flexible and stretchable when applied to the skin due to the liquefaction of gallium within the silicone encapsulant.

Figure 1C highlights representative key characteristics of TES in a rigid or soft state. TES in the rigid state is flat and stiff, is injectable into soft materials, and is able to bear high loads and hold a shape after transforming. By contrast, in the soft state, the device becomes soft, stretchable, and highly compliant, allowing it to conform to a surface and adapt to dynamic deformation. All these attributes can maximize the utility of electronics for a wide variety of different applications favoring either rigid or soft forms.

Mechanical and thermal characteristics of the transformative platform

The experimental and simulation results shown in Fig. 2 and figs. S2 to S4 summarize key characteristics of the gallium-based transformative platform with respect to materials, mechanics, and thermodynamics. Figure 2A demonstrates the concept of stiffness tuning of TES using a TES-based light-emitting diode (LED) device powered through conductive gallium wires encapsulated in soft silicone (60 kPa; Ecoflex). The device can resist weight (300 g) when the gallium is solid at room temperature but stretched by 36% as the gallium is liquefied at a temperature higher than 29.8°C. Measurements and theoretical calculations using testbed platforms (fig. S2) explore the relevant mechanical behaviors associated with the phase change of gallium (Fig. 2, B to D). Thermomechanical studies in Fig. 2B exhibit the drastic changes in the effective elastic moduli of the transformative platform at the melting temperature of gallium (29.8°C) with the tuning ratio larger than 10^4. The effective elastic moduli in the rigid state can range from 50 to 950 MPa, depending on the thickness of the gallium structure, but decreases down to ~30 kPa in the soft state where Young's modulus of liquid gallium becomes negligible. Theoretical analysis yields effective tensile moduli (Fig. 2B and fig. S2) that are well matched with the experimental values, validating the measurement accuracy. Note that the onset slope of the stress-strain curve is much steeper in the rigid state (Fig. 2C) than in the soft state (Fig. 2D) because of the large increase of the effective moduli of the samples. The samples in the rigid mode undergo plastic deformation after the short linear region because of the ductility of gallium, thus showing limited elasticity compared to the ones in the soft mode.

Thermal behaviors, which are central to the operation of the thermally driven stiffness-tuning platform, depend on the device geometry as well as the constituent materials' properties. To understand the key design parameters that dominate the thermal behavior of the transformative platform, we monitored the temperatures of testbed platforms with an infrared (IR) camera (A655sc, FLIR) during the phase transition process. Recorded temperatures during the thawing (Fig. 2, E and F) and freezing process (Fig. 2, G and H) show that gallium reaches its thawing and freezing temperature later than the silicone encapsulant primarily because of its latent heat of fusion (5.59 kJ/mol). Figure 2 (E and F) displays the temperature transient response of a testbed transformative platform during thawing, where phases I-II, II-III, and III-IV represent the solid, phase transition, and liquid state regions of gallium, respectively. If we assume that the horizontal dimensions of a sample are much larger than those of the cross-sectional dimensions, then the time required for phase transition of gallium can be expressed as $t_{transition} \propto t_{encap} \cdot t_{Ga}/(T_{th} - T_m)$, where t_{encap} is the thickness of the silicone encapsulant, t_{Ga} is the thickness of gallium, T_{th} is the thawing temperature, and T_m is the melting temperature of gallium (see note S1 for details). This analytical expression captures the experimental observations including the faster transient temperature responses at the gallium-silicone interface for thinner silicone encapsulant (Fig. 2I) as well as shorter phase transition times with increasing T_{th} (Fig. 2J). In this regard, the thermal efficiency and phase transition time in thawing (i.e., duration for II-III in Fig. 2E) in operation of transformative platforms can be improved by not only applying higher thawing temperature (T_{th}) but also reducing the thickness of both the silicone encapsulant (t_{encap}) and gallium (t_{Ga}).

Freezing shows a similar but opposite thermal behavior as shown for thawing, but undergoes an additional phase of supercooling, until nucleation of gallium is triggered below its melting temperature (Fig. 2, G and H). Heterogeneous nucleation dominates the stochastic process of nucleation during solidification, led by active heterogeneities (other solid particles in the liquid), and determines the degree of supercooling (ΔT) (*24*). As our system uses pure gallium, nucleation embryos that reside at temperatures higher than the melting temperature play a major role in nucleation of gallium. Our studies on freezing (Fig. 2K and fig. S3) show that the degree of supercooling (ΔT) required for triggering nucleation (II* in Fig. 2G) increases with the thawing temperature (T_{th}), which is the highest temperature experienced by the gallium sample when liquefied. This thermal hysteresis aligns to the precursory phenomena that nucleation embryos in liquid gallium vanish increasingly with the highest temperature experienced by the sample (*25*) and with the fact that ΔT saturates to a certain point (25°C) because of other impurities and interfacial materials (e.g., silicone encapsulants) that help nucleation (*26*). Once the nucleation of gallium is initiated, the temperature of the sample abruptly increases up to the melting temperature of gallium by releasing latent heat (see phase II*-II in Fig. 2G). Experimental studies show that the lower the nucleation temperatures (larger ΔT), the longer the time to reach the nucleation temperature (t_{c1}: I*-II*) and the shorter the phase transition time (t_{c2}: II*-III) (Fig. 2L). Overall, a larger ΔT results in an increase in the characteristic time for freezing (t_c, which is the sum of t_{c1} and t_{c2}, corresponding to phase I*-III in Fig. 2G and fig. S3G). This finding suggests the operating TES with a lower thawing temperature (T_{th}) to accelerate the soft-to-rigid transition by minimizing supercooling.

The experimental results shown in Fig. 2 (M to P) and fig. S4 explore the time required to switch transformative platforms from a rigid to soft state or from a soft to rigid state. In the thawing process, we applied T_{th} of 35°C (Fig. 2M) and 45°C (Fig. 2N), simulating body temperature or operation with an external heater, respectively. The results (Fig. 2, M and N) confirm not only a general trend of decreasing total transformation time with reduced t_{encap} and t_{Ga} but also a synergetic effect of t_{encap} and t_{Ga}, as illustrated by the analytical expression [i.e., $t_{transition} \propto t_{encap} \cdot t_{Ga}/(T_{th} - T_m)$]. In the freezing process, the characteristic time for freezing (t_c) changes similarly in relation to the device geometry, but the overall phase transition can be accelerated by lowering the freezing temperature, as demonstrated in Fig. 2 (O and P).

Multipurpose personal electronics transforming between rigid electronics and stretchable wearables

The ability of TES to tune the device stiffness and morphology enables their application in multipurpose personal electronics. Figure 3 shows a representative example of these electronics, which can be used as not only tabletop or handheld electronics but also wearable sensors according to the user's need. The TES consists of a silicone-encapsulated gallium frame (Ecoflex thickness, 500 μm; gallium thickness, 1500 μm) for rigidity tuning, a heater for accelerating the

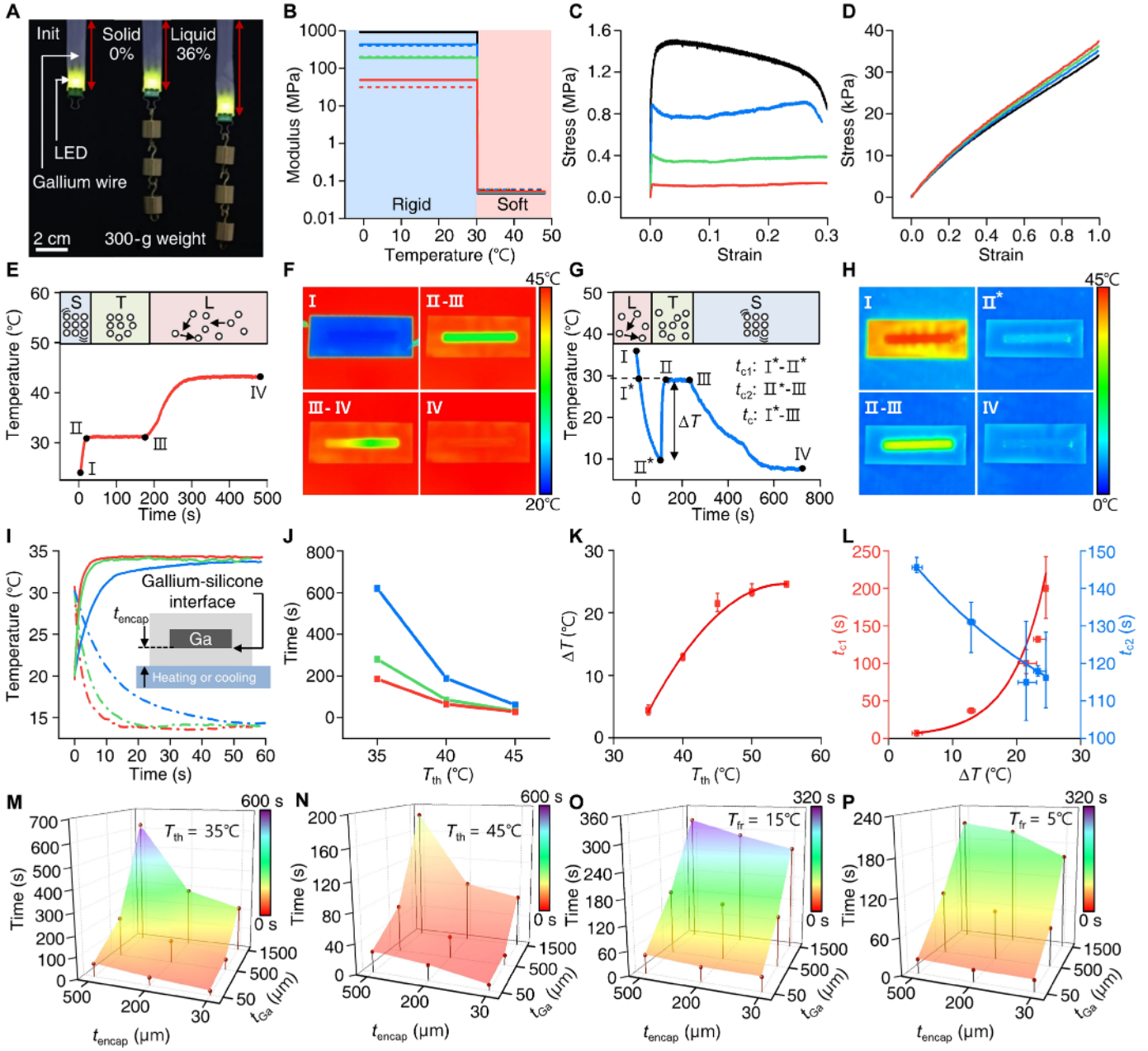

Fig. 2. Thermomechanical studies of the phase transition characteristics of the gallium-based transformative platform. (**A**) Images comparing the mechanical characteristics of a transformative LED device in a rigid (solid gallium) and soft (liquid gallium) state, powered through conductive gallium wires, when applied with a uniaxial strain by 300-g weights. (**B** to **D**) Effective elastic moduli (B) and stress-strain curves (C and D) of testbed platforms in the rigid (C) and soft state (D). Red, green, blue, and black lines in the plots indicate a testbed platform with the gallium thickness of 50, 320, 640, and 1500 μm, respectively. In all samples, the width of gallium frame is 790 μm, and the encapsulating polymer has dimensions of 5.81 mm (w) by 2.12 mm (t) (see fig. S2). The solid and dashed lines in (B) represent experimental data and theoretically calculated values, respectively. (**E** and **F**) Plot illustrating the phase transition of gallium-based transformative platform as it is thawed with a temperature of 45°C (E) and associated IR images at phases I, II-III, III-IV, and IV (F). The thawing process is divided into three phases: I-II, solid; II-III, solid-liquid transition; and III-IV, liquid. (**G** and **H**) Plot illustrating the phase transition of the gallium-based transformative platform during freezing with an applied temperature of 5°C (G) and the corresponding IR images at phases I, II*, II-III, and IV (H). The freezing process is divided into four phases: I-I*, liquid; I*-II*, supercooled liquid; II*-III, liquid-solid transition; and III-IV, solid. II* indicates a nucleation temperature. (**I**) Temperature changes at the gallium-silicone interface induced by the thawing (35°C; solid lines) and freezing temperatures (15°C; dashed lines) applied through different thicknesses of silicone encapsulants (red, 30 μm; green, 200 μm; and blue, 500 μm). (**J**) Time required for phase transition [i.e., duration for II-III in (E)] as a function of thawing temperature (T_{th}) for testbed platforms made with a 1.5-mm-thick gallium frame encapsulated in 30-μm-thick (red), 200-μm-thick (green), and 500-μm-thick (blue) silicone. (**K**) Degree of supercooling (ΔT) of gallium as a function of T_{th}. (**L**) Characteristic time for gallium to reach the nucleation temperature (t_{c1}) and time required for the phase transition (t_{c2}) as a function of ΔT during the freezing process in (G). (**M** and **N**) Time required to switch the transformative platforms (gallium thickness, 50, 500, and 1500 μm; silicone encapsulant thickness, 30, 200, and 500 μm) from the rigid to soft state when applying T_{th} of 35°C (M) and 45°C (N). (**O** and **P**) Characteristic transition time (t_c) for the transformative platform used in (M) and (N) to transform from the soft to rigid state when applying freezing temperatures (T_{fr}) of 15°C (O) and 5°C (P). Note that the soft-state platform in (O) and (N) was prepared by applying T_{th} of 35°C for 20 min before measuring t_c in freezing.

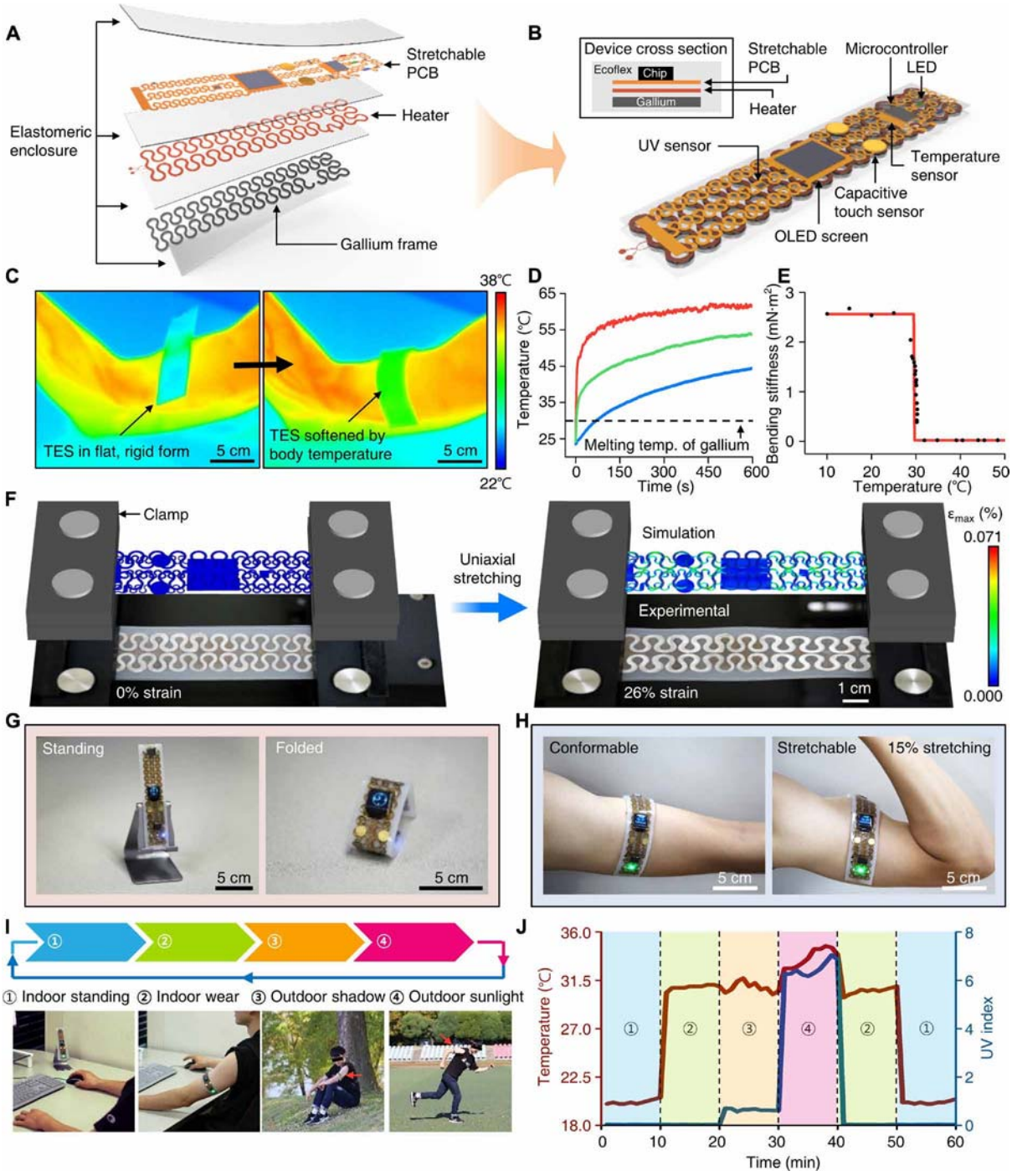

Fig. 3. Application demonstration of transformative electronics that can convert between a rigid tabletop clock and a stretchable wearable sensor. (**A**) Exploded-view schematic diagram that illustrates a TES that includes a gallium-silicone composite material as a transformative platform, a heater as an actuator for accelerated phase transition from a rigid to soft state, a stretchable PCB consisting of a temperature sensor, a UV sensor, an OLED screen, capacitive touch sensors, and a microcontroller for environmental and physiological sensing. (**B**) Illustration of the assembled device. The top inset shows a cross-sectional view. (**C**) IR images showing the mechanical transformation of the device triggered by body temperature upon mounting on the skin, which leads to conversion from a rigid, flat to soft, flexible form that enables conformal contact on the curved surface of the skin. (**D**) Temperature at the bare heater surface (red), the heater-gallium interface (green), and the device-skin interface (blue) when operating the heater with a 3.3-V coin cell battery. The operation of the heater can accelerate the phase transition of gallium while maintaining a biologically safe temperature (<45°C) at the device-skin interface. (**E**) Bending stiffness of the device as a function of temperature. (**F**) Overlay of optical images and FEA results for the device in a soft state under uniaxial strain of 0% (left) and 26% (right). (**G** and **H**) Application demonstration of the transformative electronics as a tabletop clock in the rigid mode (G) and as a wearable sensor in the soft mode (H). The sensor on the contracted arm stretched 15% because of muscle volume expansion. (**I** and **J**) Application demonstration of the device in different scenarios (I) and use of integrated sensors for the measurement of room (in a tabletop clock mode) or body temperature (in a wearable mode) and UV index for associated situations indicated by numbers (J). Photo credit: Sang-Hyuk Byun (C, F, G, and I) and Raza Qazi (H).

transformation from the rigid to soft mode, and a stretchable printed circuit board (PCB) with filamentary serpentine copper interconnects, a temperature sensor, an ultraviolet (UV) sensor, an organic LED (OLED) screen, capacitive touch sensors, and a microcontroller for multifunctional sensing and user interfaces (Fig. 3, A and B). Detailed TES dimensions, circuit design, and characterization results of the sensors are shown in fig. S5.

Placing the rigid form of the TES on the skin allows its transformation to soft, stretchable configuration, allowing the device to conform to the body surface and adapt to muscle deformation (Fig. 3C). The transformation time needed to convert the TES from the rigid to soft state can be engineered by adjusting the thawing temperature as well as thicknesses of the gallium and the silicone encapsulant (Fig. 2, M and N). Alternatively, the transformation time can be actively controlled and substantially reduced using an embedded heater (Fig. 3D). To ensure thermally safe operation on the skin while enabling relatively fast transformation, we programmed the heater to operate at ~55°C (Fig. 3D) to ensure that the temperature at the skin-silicone interface remained below the temperature at which the skin begins to burn (~45°C) (*27*). Experiments and finite element analysis (FEA) show that the bending stiffness of the TES decreases by more than two orders of magnitude (from 2.6 to 0.023 $mN{\cdot}m^2$) after transforming to the soft form (Fig. 3E and fig. S6). In addition, as shown in FEA results, in agreement with corresponding optical images of the TES (Fig. 3F), the softened TES can be stretched over 25% with only ~0.07% maximum principal strain in the polyimide/copper/polyimide system (fracture strain of copper, ~5%) due to stress-reducing effects provided by the serpentine structure, thus verifying its stretchability exceeding strain levels induced by skin deformation (10 to 20%) (*28*).

The unique ability of TES to switch between rigid and soft modes allows its versatile applications for various use cases. For example, the TES demonstrated here can be used as a tabletop clock in the rigid mode or converted to a stretchable wearable sensor for physiological and environmental monitoring (Fig. 3, G and H, and movie S1). The TES in the rigid state can also be reconfigured into diverse hard shapes to further extend its use scenarios (e.g., fully folded electronics to fit in a pocket; partially folded configuration to allow self-standing; or the flat, rigid form for handheld use). Figure 3 (I and J) shows example uses of the TES, demonstrating its potential for replacing both conventional rigid and flexible forms of electronics. This work verifies the practical and versatile utilities of the TES design, in which the individual device can function as a tabletop personal device that can display time and room temperature, as well as serve as a skin-mounted sensor to monitor the body temperature and the ambient UV index for healthcare and wellness applications.

Pressure sensor with tunable sensitivity and dynamic range

Pressure sensors are another exciting application, in which the TES concept can open new opportunities by enabling active tuning of the sensitivity and dynamic range of sensors. Recent research trends in e-skins (*29*) and wearable electronics (*30*, *31*) have focused on the development of highly sensitive pressure sensors to achieve human skin-like sophisticated sensing. Although advances in materials and micro-/nanofabrication have shown impressive accomplishments toward this goal, pressure sensors with high sensitivity are limited because of their small dynamic ranges [e.g., 0 to 10 kPa in piezoresistive or piezoelectric devices (*32*, *33*) and 0 to 100 kPa in capacitive devices (*34*, *35*)], therefore substantially restricting the spectrum of applications. A tunable pressure sensor built on a transformative platform may resolve this issue. Figure 4A illustrates a gallium-based tunable capacitive pressure sensor capable of switching between the soft mode with ultrahigh sensitivity and narrow dynamic range and the rigid mode with large dynamic range and low sensitivity. A key for the tunable pressure sensing is an active layer with variable stiffness, which is made of a gallium-elastomer composite {i.e., three-dimensional (3D) microporous elastomer [15:1 polydimethylsiloxane (PDMS)] with gallium-microdroplet inclusion; fig. S7} that presents homogeneous bulk mechanical and electrical properties. This composite design helps to circumvent problems associated with the ductile nature of the gallium frame–based design (Fig. 2C), which can cause nonlinear sensing response (fig. S8). Figure 4 (B and C) shows photographs and cross-sectional micrographs of a sensor at the rigid and soft mode under compression. By switching between the two modes by solidifying or liquefying the gallium droplets with an appropriate temperature (Fig. 2), drastic changes in deformability can be achieved (movie S2). The mechanical characterization results in Fig. 4D show that the effective modulus of the sensor can be tuned between 22 kPa (soft mode) and 9 MPa (rigid mode) through this mode switching, which is a core feature that allows the sensing characteristics to be controlled.

Figure 4E shows sensing characteristics of a pressure sensor for the soft (red) and rigid (blue) modes. As expected from the mechanical characterization results (Fig. 4D), converting between the soft and rigid mode yields large tuning of the sensitivity and dynamic range of the pressure sensor. According to the measurement, the onset sensitivity of the sensor can be tuned from 15.77 to 0.86 kPa^{-1} when switched from the soft to rigid mode, resulting in a sensitivity tuning ratio of 18.3. However, this mode switching enlarges the dynamic range [the range of applied pressure that changes (decreases) the onset sensitivity by 1%] over 12 times (from ~80 kPa to ~1.0 MPa) at the expense of the sensitivity. FEA simulations in Fig. 4F visualize the tunable nature of sensitivity of the pressure sensor to an applied pressure (50 kPa), which is enabled by controlling the effective modulus of the sensor by liquefying or solidifying the gallium droplets. Dynamic force measurements with cyclic loading and unloading (over 1000 cycles) with time-varying compressive stresses confirm that the outputs of the pressure sensor in both the rigid (Fig. 4, G and H) and soft modes (Fig. 4, K and L) are highly repeatable and reversible with no drift and very small hysteresis. The response time (10 to 90% rise time) is ~50 ms in the soft mode and ~100 ms in the rigid mode (fig. S9). The tunability along with high reproducibility of this pressure sensor makes it highly adaptable for various sensing applications. When the pressure sensor is rigid, its large dynamic range allows sensing of heavy loads, such as those generated by foot stepping (Fig. 4, I and J, and movie S3). The same sensor can be reconfigured to the soft form when it is necessary to capture gentle, sophisticated pressures, such as those associated with physiological processes, as we demonstrated by sensing carotid arterial blood pressure using the device mounted on the neck (Fig. 4, M and N). This tunable sensing platform is highly versatile. The concept presented here can also be applied for sensing a wide variety of mechanical parameters, including strain, bending, torsion, acoustics, and many others.

Deep brain neural probe that softens to match local tissue environment

While topical devices enable dynamic sensing capabilities, tissue injection expands the potential applications for biomedical devices. We

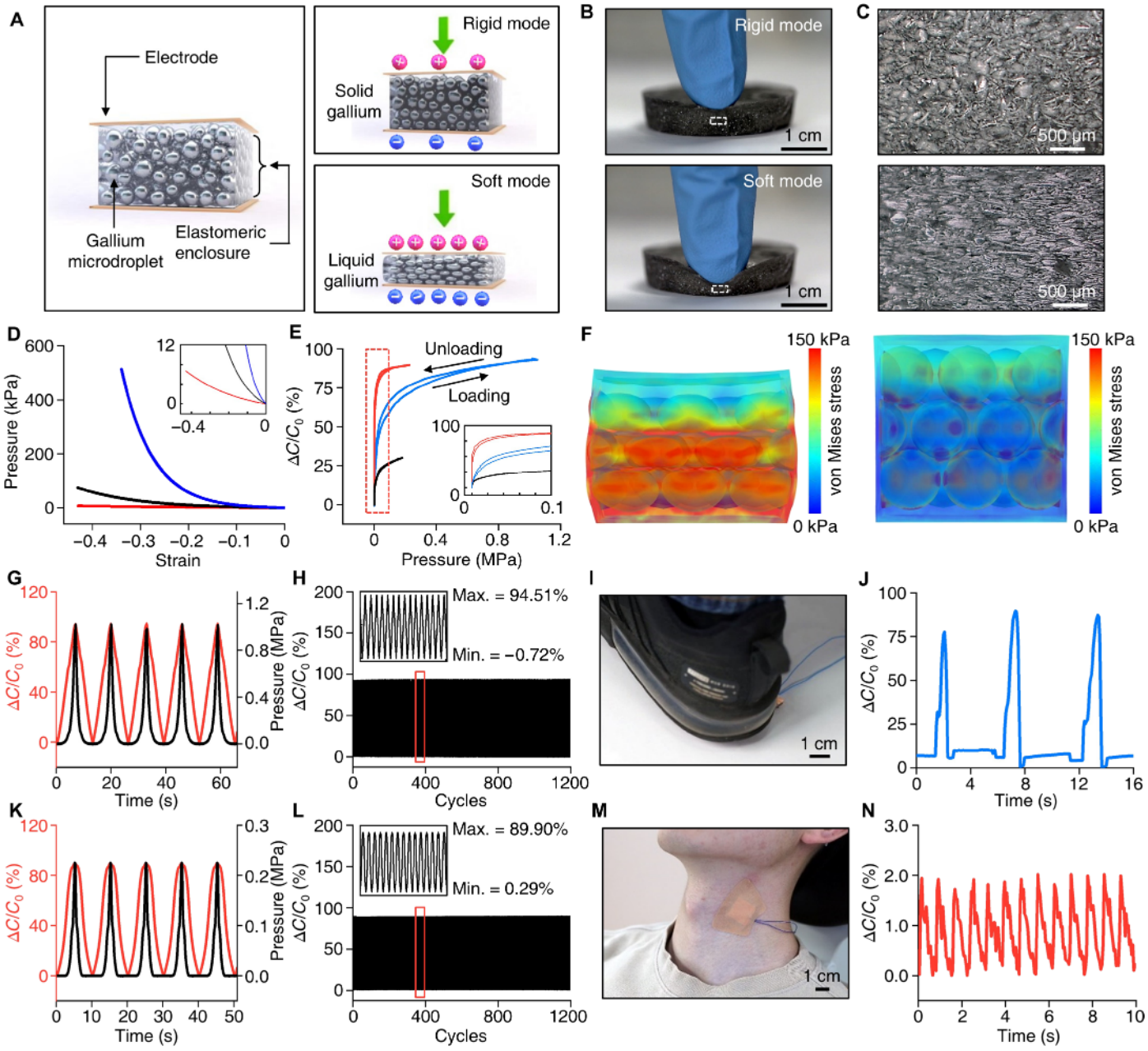

Fig. 4. Application demonstration of transformative electronics for pressure sensing, tuning both the sensitivity and dynamic range for versatile operation. (**A**) Conceptual illustration of a tunable pressure sensor based on an elastomeric composite with gallium-microdroplet inclusion. In the rigid mode, the microporous dielectric elastomer filled with solid gallium undergoes small compressive deformation due to its high effective modulus leading to large dynamic range for pressure sensing. In the soft mode, the microporous elastomer with liquefied gallium becomes much more compliant, resulting in higher sensitivity and lower dynamic range. (**B**) Photographs of a gallium-elastomer composite in the rigid (top) and soft (bottom) states under compression by a fingertip. (**C**) Cross-sectional optical micrographs of the gallium-elastomer composite in the rigid (top) and soft (bottom) states under compression, corresponding to the dotted rectangular areas in (B). (**D**) Pressure versus strain curves of the composite in the soft (red) and rigid modes (blue) in comparison to that of a pure elastomer (black). The inset shows magnified plots for the pressure range between 0 and 12 kPa. (**E**) Relative capacitance changes of the tunable pressure sensor with applied pressure in the rigid and soft modes. Red, blue, and black lines are plots for the composite in the soft and rigid modes and the pure elastomer, respectively. (**F**) FEA simulation results demonstrating the stress distribution in the composite in the soft (left) and rigid modes (right) under a compressive pressure of 50 kPa. The diameter of the gallium microdroplets is assumed to be 125 ± 50 μm (mean ± SD) based on our measurements (fig. S7E). (**G** and **K**) Cyclic capacitive response of a sensor (red) to applied pressure [1 MPa for the rigid mode (G) and 0.22 MPa for the soft mode (K); black] as a function of time in the rigid (G) and soft modes (K). The speed of loading and unloading was 0.167 mm/s in (G) and (K). (**H** and **L**) Loading and unloading test in the rigid (H) and soft (L) modes for 1200 cycles. (**I** and **J**) Image (I) and measurement result (J) demonstrating the application of a pressure sensor in the rigid mode for foot stepping pressure sensing. (**M** and **N**) Image (M) and measurement result (N) demonstrating the application of a pressure sensor in the soft mode for monitoring of carotid arterial blood pressure. Photo credit: Sang-Hyuk Byun.

recently developed injectable neural probes that rely on a releasable rigid backing needle (*3*). Figure 5 (A and B) and fig. S10 show a TES-based neural probe that circumvents this approach, similar to the ones demonstrated with shape memory polymer (*9*). It consists of a micro-inorganic LED (μ-ILED) polymeric probe [polyethylene terephthalate (PET); 6 μm] and silicone-encapsulated gallium needle (Ecoflex thickness, 30 μm; gallium thickness, 50 μm). The device remains rigid at operating room temperature (~23°C) but, upon deep brain injection, softens to help accommodate micromotions within the skull that occur during normal movement [Figs. 2B (red line) and 5B and movie S4]. The benefits of this approach can be seen after 1 month of implantation in the brain. At this time point, the TES approach has both reduced lesion size and inflammatory glial responses compared to tungsten needles of the same dimensions [600 μm (*w*) by 125 μm (*t*); Fig. 5, C to G], suggesting that the transformative approach is more amenable to deep tissue embedding.

To demonstrate functional optoelectronic interfaces on these TES neural probes, we used deep brain stimulation to drive feeding behavior in mice. Specifically, we selectively targeted ChR2(H134)-eYFP to agouti-related protein neurons of the arcuate nucleus of the hypothalamus and implanted the TES within the paraventricular hypothalamus (PVH) to stimulate a projection well known to induce hunger-related behavior (ARC^{agrp}-PVH) (Fig. 5, H and I, and fig. S10, K and L) (*36*). One hour of wireless photostimulation (20 Hz and 10-ms pulse width) of ARC^{agrp}-PVH with the TES drives increases food consumption in ad libitum fed mice (Fig. 5, J and K). The TES devices remain intact and functional for at least 6 weeks following

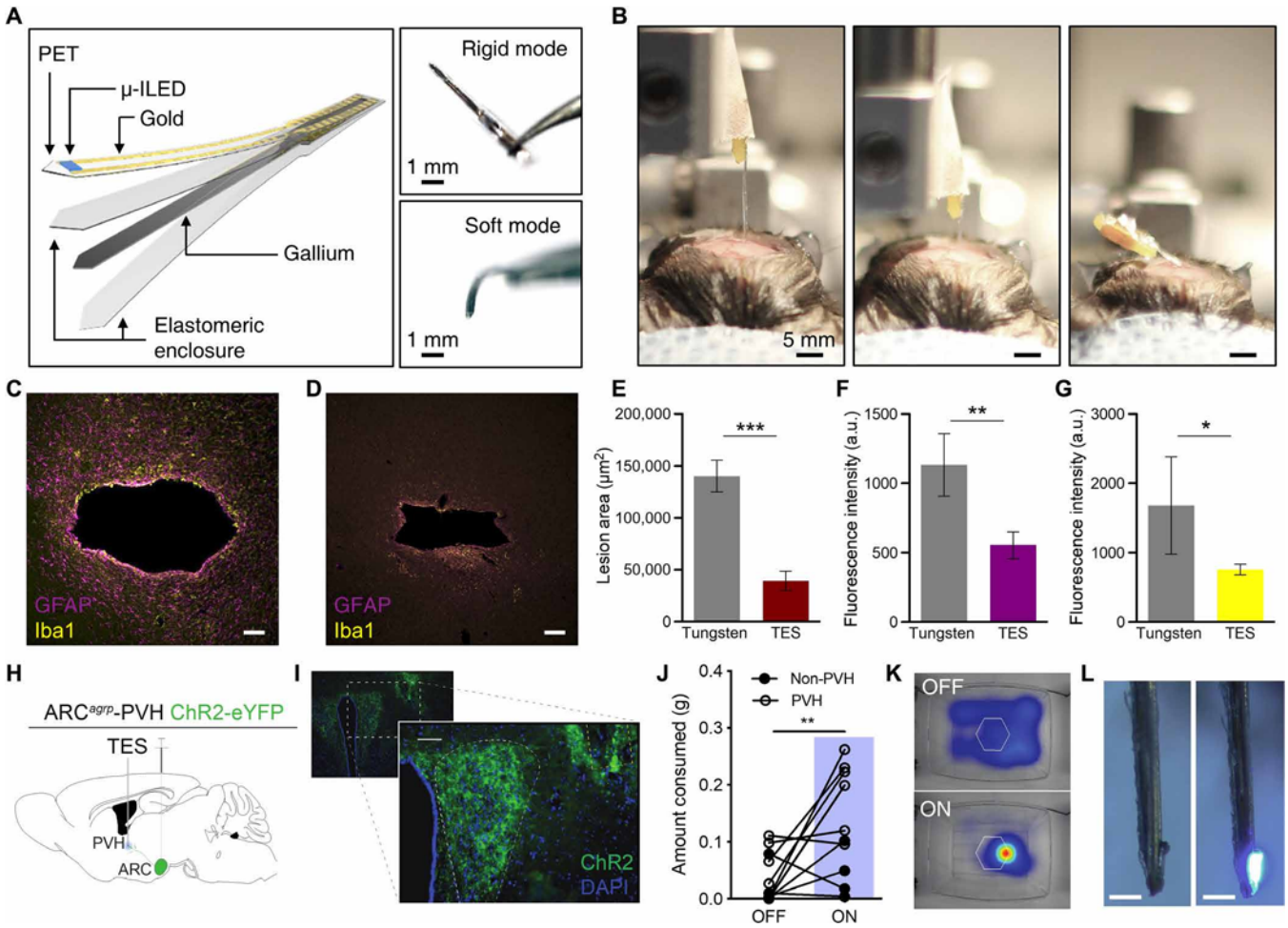

Fig. 5. Deep-tissue penetration with transformative electronics is better tolerated than rigid materials. (**A**) Conceptual illustration of the fabrication scheme (left) and photographs (right) of the TES neural probe in rigid and soft modes. (**B**) Photographs of deep brain injection of the TES-based probe in rigid (left and center) and soft (right) modes. (**C** and **D**) Fluorescence images of 35-μm horizontal slices stained for astrocytes [glial fibrillary acidic protein (GFAP), purple] and activated microglia (Iba1, yellow) from tungsten (C) and TES (D) neural probes. Scale bars, 50 μm. (**E** to **G**) Cross sections through the tissue show reduced lesion area (E) and astrocytic (F) and microglial (G) responses from the TES compared to tungsten implants following 4 weeks of implantation (data are means ± SEM, n = 3 to 5 animals per implant; *P < 0.05, **P < 0.01, ***P < 0.001, unpaired two-tailed t test). a.u., arbitrary units. (**H**) Cartoon of optogenetic and TES device targeting strategy. (**I**) Fluorescent micrograph of PVH section showing ChR2-eYFP expression (green) and TES probe implantation site (yellow dashed outline). Scale bars, 10 μm. (**J**) One hour of 20-Hz photostimulation of ARC^{AgRP}-PVH increases food consumption compared to 1 hour before stimulation [PVH: n = 6 mice, 4 AgRP-Cre × Ai32 and 2 AgRP-Cre with viral ChR2 transduction; non-PVH: n = 4; one-way analysis of variance (ANOVA) with Tukey's multiple comparisons: PVH OFF versus PVH ON, **P < 0.01; non-PVH ON versus PVH OFF, **P < 0.01]. (**K**) Example heatmap of locomotor activity near the food container (hexagon) before (top) and during (bottom) photostimulation. (**L**) Photos of a functional TES neural probe retrieved 6 weeks after implantation. Scale bars, 500 μm. Photo credit: Sang-Hyuk Byun (A), Kyle E. Parker (I), Graydon B. Gereau (C and D), and Jordan G. McCall (B and L).

deep brain implantation (Fig. 5L). Together, these findings show that TES technology can be readily adapted for deep tissue integration and that these approaches might be better tolerated by the surrounding tissues.

DISCUSSION

The concepts, materials, and design strategies presented here enable mechanically transformable electronics that can break the boundary between traditional rigid electronics and more recent soft wearable devices. TES are universal electronic platforms compatible with many modern flexible/stretchable electronics made of organic and inorganic materials. Gallium is a core base material for the TES design, which allows tuning of the shape and stiffness of electronics through the body temperature, opening opportunities for wearable and implantable electronics. Supercooling caused in freezing of gallium is deleterious to high-precision control of TES, but the degree of supercooling can be minimized by adding nucleating agents or impurities (*37*). For applications requiring different transition temperatures, other types of fusible alloys (*38*) are available for the replacement of gallium. In all cases, integration of thin, flexible thermoelectronics with the TES design could notably facilitate rapid bidirectional transformation (i.e., from rigid to soft or vice versa) and thus further expand the potential of this system for a wide variety of electronics, including consumer electronics, biomedical devices, soft robotics, and many others. For reliable and durable operation, materials and packaging schemes that provide robust sealing of phase change metals (i.e., gallium or other fusible alloys) will need to be further developed.

MATERIALS AND METHODS

Fabrication of gallium frame–based TESs

The fabrication started with 3D printing (Core 530, B9 Creations) of a casting mold with a desired frame pattern thickness using a stereolithographic process on a UV curable photopolymer (B9R-4-Yellow, B9Creations). It was chemically treated with an anti-stiction agent (chlorotrimethylsilane; Sigma-Aldrich); then, PDMS (SYLGARD 184, Dow Corning) was casted on the mold. Once curing of PDMS (60 min at 70°C) was completed, the PDMS layer was delaminated from the 3D-printed mold to use it as a casting mold for a gallium frame. Liquid gallium (Ga metal 99.99, RotoMetals) was then casted on the PDMS mold and clamped tightly with a glass slide (75 mm by 50 mm by 1 mm). Subsequently, the gallium was solidified at 5°C by placing the sample on a cool plate (CP-200TT, TE Technology) to create a solid gallium frame. The gallium frame was carefully released from the mold and encapsulated with silicone (Ecoflex 00-30, Smooth-On) to form a transformative platform. Last, the fabrication of transformative electronics was completed by integrating a separately fabricated flexible and/or stretchable electronics onto this transformative platform. Details on fabrication of flexible and/or stretchable electronics attached on the transformative platforms, which appeared in Figs. 1, 3, and 5, can be found in notes S2 to S4.

Fabrication of tunable pressure sensor based on gallium-elastomer composite

The tunable pressure sensor (Fig. 4) was fabricated by creating gallium microdroplets dispersed in a silicone elastomer (PDMS SYLGARD 184, Dow Corning) in a similar fashion reported by Bartlett *et al.* (*39*). First, the prepolymer of PDMS with 15:1 elastomer:curing agent weight ratio was prepared. Then, the gallium-elastomer composite was made by shear mixing the uncured PDMS and liquid gallium at a volume ratio of 1:1 with a mortar and pestle. Gallium and PDMS were mixed for ~10 min until it became a homogeneous viscous composite, and subsequently, the composite was cured at 70°C for 60 min. Last, indium tin oxide (ITO)–covered PET substrates (0.175 mm thick, 50 ohms per square, ITO-coated PET 1309; Adafruit) or copper foil (60 μm thick; Seogwang Chemical) was integrated at the top and bottom of the composite to complete a capacitive pressure sensor.

Elastic modulus measurement

The elastic modulus was measured using a dynamic mechanical analyzer (DMA) (TA@DMA Q800). Samples were tested in the DMA chamber for accurate temperature control during the modulus measurements. The frequency of loading used in this test was set to low (0.1 Hz) to eliminate influence of the viscosity of silicone for the mechanical characterization. During the measurement, the temperature of the DMA chamber was increased slowly from 0° to 50°C with a rate of 0.5°C/min to allow enough heating time for the samples to reach steady state.

Stress-strain curve measurement

The stress-strain curves for transformative platforms in rigid and soft state were obtained using an Instron Mechanical Testing system. Testbed samples, prepared by encapsulating a gallium structure with silicone (Ecoflex, Smooth-On), were made into a "dog bone" shape (fig. S2) so that 3D-printed triangular plastic pieces securely hold a sample at its both ends to apply force only to the sample body during mechanical testing. The force and displacement information measured by the machine were used to calculate stress and strain. For measurements in soft state, gallium was first melted by applying temperature higher than its melting temperature. Then, for each type of the transformative platforms, three samples were measured and averaged for the stress-strain curve. Subsequently, the same batch of samples was cooled down with liquid nitrogen, turning gallium into solid state. After stabilizing the samples at room temperature, the same mechanical measurements were carried out to obtain stress-strain curves at rigid state.

Bending stiffness measurement

Bending stiffness of transformative electronics was obtained by measuring its deflection according to applied force. For measurements, one end of the device was clamped, while the other end was applied with a 10-g weight. Deflection due to its own weight and the applied weight was measured using an optical camera by increasing the temperature by 0.1°C from 10° to 50°C. Then, the bending stiffness (EI) was calculated using the equation $EI = FL^3/3z$, where F, z, and L indicate the applied force, deflection, and length of the beam, respectively. For accurate temperature control, all the measurements were done in a constant temperature chamber (HQ-DTH, Coretech).

Mechanical modeling and FEA

A commercial FEA software (Abaqus, Dassault Systèmes) was used for simulating the deformation of the device to obtain strain information for the transformative electronics in Fig. 3. In the simulation, the polyimide and chip layers were simulated using four-node shell elements (S4R), and the remaining materials were simulated using eight-node, 3D hexahedron elements (C3D8R). The effective

moduli of the device in soft and rigid state were also obtained by applying a 1% strain and measuring the reaction force at both ends to the device.

Characterization of a pressure sensor

A pressure sensor was characterized by measuring applied force and resulting capacitance changes using a force gauge (Series 5, Mark-10) and an LCR meter (4284A Precision LCR Meter, Hewlett Packard), respectively. The sensor was placed on a mechanical test platform (ESM303, Mark-10), and the force was applied perpendicularly to the sensor with a rate of 10 mm/min. The applied pressure was calculated by dividing the measured force by the contact area. The effective modulus of the gallium-elastomer composite was calculated by the slope of the stress versus strain curve. The dynamic range of the sensor was calculated by the applied pressure until the sensitivity is lower than 1% of the onset sensitivity. A custom-developed LabVIEW software was used for automated measurements of capacitance changes per applied pressure.

Experiments on human subjects

All experiments on human skins were performed under approval from the Institutional Review Board at Korea Advanced Institute of Science and Technology (protocol number: KH2018-35) and received informed consent from the volunteer subjects.

Experimental on animal subjects

Adult (20 to 30 g) male C57BL/6J and *agrp*-IRES-Cre (*40*) backcrossed to C57BL/6J mice and bred to Ai32 mice (*41*) were group-housed, given access to food pellets and water ad libitum, and maintained on a 12-hour:12-hour light:dark cycle (lights on at 6:00 a.m.). All mice were transferred to a facility within the laboratory after weaning and remained in the facility in the laboratory at least 1 week before surgery, after surgery, and throughout the duration of the behavioral assays to minimize stress from transportation and disruption from foot traffic. All procedures were approved by the Animal Care and Use Committee of Washington University and conformed to U.S. National Institutes of Health (NIH) guidelines.

Stereotaxic surgery

Neural probes were implanted as previously described (*3*, *42*) with minor modifications to accommodate the TES probe described here. Briefly, after the mice were acclimatized to the holding facility for 7 to 21 days, they were anaesthetized in an induction chamber (4% isoflurane) and placed in a stereotaxic frame (model 942, Kopf Instruments), where they were maintained at 1 to 2% isoflurane. A standard cannula holder (model 1776-P1, Kopf Instruments) was adapted to implant the TES and tungsten devices. TES and tungsten devices were ethanol-sterilized and kept on ice until immediately before the implantation to avoid any melting. The implants were secured with C&B Metabond (Parkell). For the glial response studies, mice were implanted with either tungsten or TES probes in the dorsal striatum [stereotaxic coordinates from bregma: anterior-posterior (AP), +1.10 mm; medial-lateral (ML), ±1.50 mm; dorsal-ventral (DV), −4.00 mm]. For the optogenetic feeding experiment, agrp-IRES-Cre mice were injected with 400 nl of AAV5-EF1a-ChR2(H134)-eYFP (Addgene) unilaterally into the ARC (stereotaxic coordinates from bregma: AP, −1.5 mm; ML, −0.2 mm; DV, −5.8 mm). Three weeks later, agrp-IRES-Cre mice or agrp-IRES-Cre × Ai32 mice were then implanted with the TES device adjacent to the PVH (stereotaxic coordinates from bregma: AP, −0.82 mm; ML, −0.5 mm; DV, −5.25 mm). C57BL/6J mice were allowed to recover for 14 to 31 days before testing. *agrp*-IRES-Cre mice were allowed to recover 3 weeks following viral injection to permit optimal expression at ARC^{agrp}-PVH terminals. *agrp*-IRES-Cre and *agrp*-IRES-Cre × Ai32 mice were allowed to recover 1 week following the TES implant before behavior.

Immunohistochemistry

Immunohistochemistry was performed as described (*3*). Briefly, mice were anesthetized with a ketamine/xylazine/acepromazine cocktail and intracardially perfused with paraformaldehyde in phosphate-buffered saline (PBS). Brains were dissected, postfixed for 24 hours at 4°C, cryoprotected with solution of 30% sucrose in 0.1 M phosphate buffer (PB) at 4°C for at least 24 hours, cut into 35-μm sections, and processed for immunostaining. Brain sections (35 μm) were washed three times in PBS and blocked in PBS containing 0.5% Triton X-100 and 5% normal goat serum. For glial responses in implanted tissues, horizontal sections were then incubated for ~16 hours at room temperature in guinea pig anti-GFAP (glial fibrillary acidic protein) (1:500; Synaptic Systems) and rabbit anti-Iba1 (1:300; Wako Chemicals). Following incubation, sections were washed three times in PBS and incubated for 2 hours at room temperature in Alexa Fluor 488 goat anti-rabbit immunoglobulin G (1:1000; Invitrogen) and goat anti–guinea pig Alexa Fluor 546 (1:1000; Invitrogen), washed three times in PBS and incubated for 1 hour in NeuroTrace 435/455 Blue Fluorescent Nissl stain (1:400), and then washed three times in PBS, followed by three 10-min washes in PB, and mounted on glass slides with HardSet Vectashield (Vector Laboratories). For tissue from the feeding studies, sections were washed three times in PBS, followed by three 10-min washes in PB, and mounted on glass slides with HardSet Vectashield with 4′,6-diamidino-2-phenylindole (DAPI) (Vector Laboratories). All sections were imaged on an epifluorescent microscope, and z-stacks were taken throughout the focal plane. 3D deconvolution was then performed, and images are presented as a maximum projection of that 3D deconvolution. Gain and exposure time were constant throughout each experiment, and all image groups were processed in parallel and analyzed using ImageJ (NIH).

Food consumption behavior

The food intake study was performed at the onset of the light cycle as previously described (*36*). All animals were singly housed for at least 2 weeks following surgery and handled daily to ensure acclimation and minimize any stress response to experimental procedures. On test day, Bluetooth-connected battery packs were attached to each animal's intracranial TES device implant. Animals were then placed in a large (rat-style) polycarbonate cage and allowed to acclimate to the environment for 1 hour. After 1 hour, one pellet of standard laboratory chow (~4 g) was placed on a weigh boat fixed to the cage center. Following 1 hour of food access, the food was weighed and immediately placed in the cage center. Next, mice received blue μ-ILED photostimulation at 20 Hz for 1 hour, and the food was weighed immediately after. Locomotor and position data were monitored with EthoVision (Noldus). Mice with implantation outside the PVH or lacked PVH ChR2 expression were excluded from the group after histological examination by a separate experimenter and reported here as non-PVH animals. By this process, all food intake measurements were randomized and blind to the experimenter.

Statistical and data analysis

Fitting lines in Fig. 2 (K and L) were produced with polynomial function and exponential function, respectively. Data displayed in Fig. 2K and fig. S3G correspond to an average of the degree of supercooling (ΔT) with SD. Data displayed in Fig. 2L correspond to an average of characteristic time for gallium to reach nucleation temperature (t_{c1}) and time required for phase transition (t_{c2}) with SD of t_{c1} and t_{c2}, respectively. Data in Fig. 5 (E to G) are expressed as means ± SEM. Data were normally distributed by Shapiro-Wilk, and differences between groups were determined using independent *t* tests. Data in Fig. 5J were analyzed with one-way analysis of variance (ANOVA) followed by Tukey's multiple comparisons. All data were processed using OriginLab or Prism 8 (GraphPad).

SUPPLEMENTARY MATERIALS

Supplementary material for this article is available at http://advances.sciencemag.org/cgi/content/full/5/11/eaay0418/DC1

Note S1. Theoretical analysis of phase transition time for thawing
Note S2. Fabrication of transformative electronics with flexible, stretchable electrode arrays
Note S3. Fabrication of transformative electronics integrated with a stretchable PCB
Note S4. Fabrication of neural probe with variable stiffness
Fig. S1. Design and application of a transformative electronics that can convert between an EMG sensor and a handheld touch sensor.
Fig. S2. Design of testbed transformative platforms for mechanical studies.
Fig. S3. Characterization of the degree of supercooling.
Fig. S4. Thermal characterization of gallium-based transformative platform using IR camera during thawing process and freezing process.
Fig. S5. Design of transformative electronics that can convert between a rigid tabletop clock and a stretchable wearable sensor with characterization.
Fig. S6. Mechanical simulation of bending stiffness of the transformative electronics that appeared in Fig. 3E.
Fig. S7. Fabrication process of a transformative pressure sensor.
Fig. S8. Transformative resistive pressure sensor built with a gallium frame.
Fig. S9. Response time of the pressure sensor in rigid and soft mode.
Fig. S10. Design and implementation of TES optical neural probe for behavioral experiments with wireless control.
Movie S1. Movie of a transformative electronics transforming between a rigid tabletop clock and a wearable sensor.
Movie S2. Movie of a transformative pressure sensor with variable deformability.
Movie S3. Movie of a transformative pressure sensor: Application demonstration in rigid and soft modes.
Movie S4. Movie of a transformative neural probe penetrating a mouse brain in rigid mode.

REFERENCES AND NOTES

1. D.-H. Kim, N. Lu, R. Ma, Y.-S. Kim, R.-H. Kim, S. Wang, J. Wu, S. M. Won, H. Tao, A. Islam, K. J. Yu, T. Kim, R. Chowdhury, M. Ying, L. Xu, M. Li, H.-J. Chung, H. Keum, M. McCormick, P. Liu, Y.-W. Zhang, F. G. Omenetto, Y. Huang, T. Coleman, J. A. Rogers, Epidermal electronics. Science **333**, 838–843 (2011).
2. M. Kaltenbrunner, T. Sekitani, J. Reeder, T. Yokota, K. Kuribara, T. Tokuhara, M. Drack, R. Schwödiauer, I. Graz, S. Bauer-Gogonea, S. Bauer, T. Someya, An ultra-lightweight design for imperceptible plastic electronics. Nature **499**, 458–463 (2013).
3. J.-W. Jeong, J. G. McCall, G. Shin, Y. Zhang, R. Al-Hasani, M. Kim, S. Li, J. Y. Sim, K.-I. Jang, Y. Shi, D. Y. Hong, Y. Liu, G. P. Schmitz, L. Xia, Z. He, P. Gamble, W. Z. Ray, Y. Huang, M. R. Bruchas, J. A. Rogers, Wireless optofluidic systems for programmable in vivo pharmacology and optogenetics. Cell **162**, 662–674 (2015).
4. K. N. Noh, S. I. Park, R. Qazi, Z. Zou, A. D. Mickle, J. G. Grajales-Reyes, K.-I. Jang, R. W. Gereau IV, J. Xiao, J. A. Rogers, J.-W. Jeong, Miniaturized, battery-free optofluidic systems with potential for wireless pharmacology and optogenetics. Small **14**, 1702479 (2018).
5. I. R. Minev, P. Musienko, A. Hirsch, Q. Barraud, N. Wenger, E. M. Moraud, J. Gandar, M. Capogrosso, T. Milekovic, L. Asboth, R. F. Torres, N. Vachicouras, Q. Liu, N. Pavlova, S. Duis, A. Larmagnac, J. Vörös, S. Micera, Z. Suo, G. Courtine, S. P. Lacour, Electronic dura mater for long-term multimodal neural interfaces. Science **347**, 159–163 (2015).
6. S. Wang, J. Xu, W. Wang, G.-J. N. Wang, R. Rastak, F. Molina-Lopez, J. W. Chung, S. Niu, V. R. Feig, J. Lopez, T. Lei, S.-K. Kwon, Y. Kim, A. M. Foudeh, A. Ehrlich, A. Gasperini, Y. Yun, B. Murmann, J. B.-H. Tok, Z. Bao, Skin electronics from scalable fabrication of an intrinsically stretchable transistor array. Nature **555**, 83–88 (2018).
7. K. Takashima, K. Sugitani, N. Morimoto, S. Sakaguchi, T. Noritsugu, T. Mukai, Pneumatic artificial rubber muscle using shape-memory polymer sheet with embedded electrical heating wire. Smart Mater. Struct. **23**, 125005 (2014).
8. A. Avendano-Bolivar, T. Ware, D. Arreaga-Salas, D. Simon, W. Voit, Mechanical cycling stability of organic thin film transistors on shape memory polymers. Adv. Mater. **25**, 3095–3099 (2013).
9. T. Ware, D. Simon, D. E. Arreaga-Salas, J. Reeder, R. Rennaker, E. W. Keefer, W. Voit, Fabrication of responsive, softening neural interfaces. Adv. Funct. Mater. **22**, 3470–3479 (2012).
10. B. E. Schubert, D. Floreano, Variable stiffness material based on rigid low-melting-point-alloy microstructures embedded in soft poly(dimethylsiloxane) (PDMS). RSC Adv. **3**, 24671–24679 (2013).
11. A. Tonazzini, S. Mintchev, B. Schubert, B. Mazzolai, J. Shintake, D. Floreano, Variable stiffness fiber with self-healing capability. Adv. Mater. **28**, 10142–10148 (2016).
12. W. Shan, T. Lu, C. Majidi, Soft-matter composites with electrically tunable elastic rigidity. Smart Mater. Struct. **22**, 085005 (2013).
13. I. M. Van Meerbeek, B. C. Mac Murray, J. W. Kim, S. S. Robinson, P. X. Zou, M. N. Silberstein, R. F. Shepherd, Morphing metal and elastomer bicontinuous foams for reversible stiffness, shape memory, and self-healing soft machines. Adv. Mater. **28**, 2801–2806 (2016).
14. Tunable elastic stiffness with microconfined magnetorheological domains at low magnetic field. Appl. Phys. Lett. **97**, 164104 (2010).
15. Z. Varga, G. Filipcsei, M. Zrínyi, Magnetic field sensitive functional elastomers with tuneable elastic modulus. Polymer **47**, 227–233 (2006).
16. S. B. Behbahani, X. Tan, Design and dynamic modeling of electrorheological fluid-based variable-stiffness fin for robotic fish. Smart Mater. Struct. **26**, 085014 (2017).
17. A. Balasubramanian, M. Standish, C. J. Bettinger, Microfluidic thermally activated materials for rapid control of macroscopic compliance. Adv. Funct. Mater. **24**, 4860–4866 (2014).
18. N. G. Cheng, A. Gopinath, L. Wang, K. Iagnemma, A. E. Hosoi, Thermally tunable, self-healing composites for soft robotic applications. Macromol. Mater. Eng. **299**, 1279–1284 (2014).
19. L. Wang, Y. Yang, Y. Chen, C. Majidi, F. Iida, E. Askounis, Q. Pei, Controllable and reversible tuning of material rigidity for robot applications. Mater. Today **21**, 563–576 (2018).
20. H. Gao, J. Li, F. Zhang, Y. Liu, J. Leng, The research status and challenges of shape memory polymer-based flexible electronics. Mater. Horiz. **6**, 931–944 (2019).
21. Y. Lu, Q. Hu, Y. Lin, D. B. Pacardo, C. Wang, W. Sun, F. S. Ligler, M. D. Dickey, Z. Gu, Transformable liquid-metal nanomedicine. Nat. Commun. **6**, 10066 (2015).
22. M. D. Dickey, Stretchable and soft electronics using liquid metals. Adv. Mater. **29**, 1606425 (2017).
23. J. Shintake, B. Schubert, S. Rosset, H. Shea, D. Floreano, Variable stiffness actuator for soft robotics using dielectric elastomer and low-melting-point alloy, in 2015 IEEE/RSJ International Conference on Intelligent Robots and Systems (IROS) (IEEE, 2015), pp. 1097–1102.
24. H. Fredriksson, U. Åkerlind, Solidification and Crystallization Processing in Metals and Alloys (John Wiley & Sons, 2012).
25. M. Kano, Supercooling and its thermal hysteresis of pure metal liquids. Netsu Sokutei **18**, 64–70 (1991).
26. B. Chalmers, Principles of Solidification (Wiley, 1964).
27. Y.-J. Lue, H.-H. Wang, K.-I. Cheng, C.-H. Chen, Y.-M. Lu, Thermal pain tolerance and pain rating in normal subjects: Gender and age effects. Eur. J. Pain **22**, 1035–1042 (2018).
28. N. Lu, C. Lu, S. Yang, J. Rogers, Highly sensitive skin-mountable strain gauges based entirely on elastomers. Adv. Funct. Mater. **22**, 4044–4050 (2012).
29. M. L. Hammock, A. Chortos, B. C.-K. Tee, J. B.-H. Tok, Z. Bao, 25th anniversary article: The evolution of electronic skin (E-Skin): A brief history, design considerations, and recent progress. Adv. Mater. **25**, 5997–6038 (2013).
30. Y. Gao, H. Ota, E. W. Schaler, K. Chen, A. Zhao, W. Gao, H. M. Fahad, Y. Leng, A. Zheng, F. Xiong, C. Zhang, L.-C. Tai, P. Zhao, R. S. Fearing, A. Javey, Wearable microfluidic diaphragm pressure sensor for health and tactile touch monitoring. Adv. Mater. **29**, 1701985 (2017).
31. W. Wu, X. Wen, Z. L. Wang, Taxel-addressable matrix of vertical-nanowire piezotronic transistors for active and adaptive tactile imaging. Science **340**, 952–957 (2013).
32. L. Pan, A. Chortos, G. Yu, Y. Wang, S. Isaacson, R. Allen, Y. Shi, R. Dauskardt, Z. Bao, An ultra-sensitive resistive pressure sensor based on hollow-sphere microstructure induced elasticity in conducting polymer film. Nat. Commun. **5**, 3002 (2014).
33. K. Meng, J. Chen, X. Li, Y. Wu, W. Fan, Z. Zhou, Q. He, X. Wang, X. Fan, Y. Zhang, J. Yang, Z. L. Wang, Flexible weaving constructed self-powered pressure sensor enabling continuous diagnosis of cardiovascular disease and measurement of cuffless blood pressure. Adv. Funct. Mater. **29**, 1806388 (2019).
34. C. M. Boutry, Y. Kaizawa, B. C. Schroeder, A. Chortos, A. Legrand, Z. Wang, J. Chang, P. Fox, Z. Bao, A stretchable and biodegradable strain and pressure sensor for orthopaedic application. Nat. Electron. **1**, 314–321 (2018).

35. J.-O. Kim, S. Y. Kwon, Y. Kim, H. B. Choi, J. C. Yang, J. Oh, H. S. Lee, J. Y. Sim, S. Ryu, S. Park, Highly ordered 3d microstructure-based electronic skin capable of differentiating pressure, temperature, and proximity. ACS Appl. Mater. Interfaces **11**, 1503–1511 (2019).
36. D. Atasoy, J. N. Betley, H. H. Su, S. M. Sternson, Deconstruction of a neural circuit for hunger. Nature **488**, 172–177 (2012).
37. S. A. Kozlov, N. A. Potolokov, A. V. Gusev, V. A. Fedorov, Effect of impurities on crystal growth of gallium. Inorg. Mater. **39**, 1267–1270 (2003).
38. H. Ge, H. Li, S. Mei, J. Liu, Low melting point liquid metal as a new class of phase change material: An emerging frontier in energy area. Renew. Sustain. Energy Rev. **21**, 331–346 (2013).
39. M. D. Bartlett, N. Kazem, M. J. Powell-Palm, X. Huang, W. Sun, J. A. Malen, C. Majidi, High thermal conductivity in soft elastomers with elongated liquid metal inclusions. Proc. Natl. Acad. Sci. U.S.A. **114**, 2143–2148 (2017).
40. Q. Tong, C.-P. Ye, J. E. Jones, J. K. Elmquist, B. B. Lowell, Synaptic release of GABA by AgRP neurons is required for normal regulation of energy balance. Nat. Neurosci. **11**, 998–1000 (2008).
41. L. Madisen, T. Mao, H. Koch, J. Zhuo, A. Berenyi, S. Fujisawa, Y.-W. A. Hsu, A. J. Garcia Iii, X. Gu, S. Zanella, J. Kidney, H. Gu, Y. Mao, B. M. Hooks, E. S. Boyden, G. Buzsáki, J. M. Ramirez, A. R. Jones, K. Svoboda, X. Han, E. E. Turner, H. Zeng, A toolbox of Cre-dependent optogenetic transgenic mice for light-induced activation and silencing. Nat. Neurosci. **15**, 793–802 (2012).
42. J. G. McCall, R. Qazi, G. Shin, S. Li, M. H. Ikram, K.-I. Jang, Y. Liu, R. Al-Hasani, M. R. Bruchas, J.-W. Jeong, J. A. Rogers, Preparation and implementation of optofluidic neural probes for in vivo wireless pharmacology and optogenetics. Nat. Protoc. **12**, 219–237 (2017).

Acknowledgments: We thank the Organic and Nano Electronics Laboratory (Steve Park Research Group) in the Department of Materials Science and Engineering at KAIST for providing measuring apparatuses for characterization of pressure sensors. **Funding:** This work was supported by the Basic Science Research Program and the BK21 Plus Program through the National Research Foundation of Korea (NRF) funded by the Ministry of Science and ICT (NRF-2018R1C1B6001706 and NRF-2018025230 to J.-W.J.), the U.S. NIH (R25 MH112473 to J.B.), and the Oak Ridge Associated Universities (J.G.M.). **Author contributions:** Concept, design, and study direction: S.-H.B., J.Y.S., and J.-W.J.; device fabrication: S.-H.B., J.Y.S., R.Q., M.P.H., A.S., and S.L.; experimental validation: S.-H.B., J.Y.S., Z.Z., J.L., R.Q., M.C.W., K.E.P., M.P.H., S.H.C., A.S., G.B.G., S.L., Y.L., W.-H.Y., J.G.M., J.X., and J.-W.J.; data analysis: S.-H.B., J.Y.S., Z.Z., M.C.W., K.E.P., J.B., J.G.M., J.X., and J.-W.J.; theoretical modeling: S.-H.B., J.Y.S., Z.Z., and J.X.; manuscript writing: S.-H.B., J.Y.S., Z.Z., K.E.P., J.G.M., J.X., and J.-W.J.; supervision: J.G.M., J.X., and J.-W.J.; projection administration: J.-W.J. **Competing interests:** The authors declare that they have no competing interests. **Data and materials availability:** All data needed to evaluate the conclusions in the paper are present in the paper and/or the Supplementary Materials. Any additional datasets, analysis details, and material recipes are available upon request.

Submitted 14 May 2019
Accepted 14 September 2019
Published 1 November 2019
10.1126/sciadv.aay0418

Citation: S.-H. Byun, J. Y. Sim, Z. Zhou, J. Lee, R. Qazi, M. C. Walicki, K. E. Parker, M. P. Haney, S. H. Choi, A. Shon, G. B. Gereau, J. Bilbily, S. Li, Y. Liu, W.-H. Yeo, J. G. McCall, J. Xiao, J.-W. Jeong, Mechanically transformative electronics, sensors, and implantable devices. Sci. Adv. **5**, eaay0418 (2019).

Mechanically transformative electronics, sensors, and implantable devices

Sang-Hyuk Byun, Joo Yong Sim, Zhanan Zhou, Juhyun Lee, Raza Qazi, Marie C. Walicki, Kyle E. Parker, Matthew P. Haney, Su Hwan Choi, Ahnsei Shon, Graydon B. Gereau, John Bilbily, Shuo Li, Yuhao Liu, Woon-Hong Yeo, Jordan G. McCall, Jianliang Xiao and Jae-Woong Jeong

Sci Adv **5** (11), eaay0418.
DOI: 10.1126/sciadv.aay0418